

Sulfur-doped graphene nanoribbons with a sequence of distinct band gaps

Yan-Fang Zhang^{1,5,§}, Yi Zhang^{1,§}, Geng Li¹, Jianchen Lu¹, Yande Que¹, Hui Chen¹, Reinhard Berger^{2,3}, Xinliang Feng^{3,4} (✉), Klaus Müllen², Xiao Lin¹, Yu-Yang Zhang^{1,5}, Shixuan Du¹ (✉), Sokrates T. Pantelides^{5,1}, and Hong-Jun Gao¹

¹ Institute of Physics & University of Chinese Academy of Sciences, Chinese Academy of Sciences, Beijing 100190, China

² Max Planck Institute for Polymer Research, Ackermannweg 10, D-55128 Mainz, Germany

³ Center for Advancing Electronics Dresden (cfaed) & Department of Chemistry and Food Chemistry, Technische Universität Dresden, D-01069 Dresden, Germany

⁴ School of Chemistry and Chemical Engineering, Shanghai Jiao Tong University, Shanghai 200240, China

⁵ Department of Physics and Astronomy and Department of Electrical Engineering and Computer Science, Vanderbilt University, Nashville, Tennessee 37235, USA

[§] Yan-Fang Zhang and Yi Zhang contributed equally to this work.

Received: 27 December 2016

Revised: 20 February 2017

Accepted: 23 February 2017

© Tsinghua University Press and Springer-Verlag Berlin Heidelberg 2017

KEYWORDS

bottom-up fabrication, chevron-type graphene nanoribbons, nanoscale quantum dots, scanning tunneling microscopy, density functional theory

ABSTRACT

Unlike graphene sheets, graphene nanoribbons (GNRs) can exhibit semiconducting band gap characteristics that can be tuned by controlling impurity doping and the GNR widths and edge structures. However, achieving such control is a major challenge in the fabrication of GNRs. Chevron-type GNRs were recently synthesized via surface-assisted polymerization of pristine or N-substituted oligophenylene monomers. In principle, GNR heterojunctions can be fabricated by mixing two different monomers. In this paper, we report the fabrication and characterization of chevron-type GNRs using sulfur-substituted oligophenylene monomers to produce GNRs and related heterostructures for the first time. First-principles calculations show that the GNR gaps can be tailored by applying different sulfur configurations from cyclodehydrogenated isomers via debromination and intramolecular cyclodehydrogenation. This feature should enable a new approach for the creation of multiple GNR heterojunctions by engineering their sulfur configurations. These predictions have been confirmed via scanning tunneling microscopy and scanning tunneling spectroscopy. For example, we have found that the S-containing GNRs contain segments with distinct band gaps, i.e., a sequence of multiple heterojunctions that results in a sequence of quantum dots. This unusual intraribbon heterojunction sequence may be useful in nanoscale optoelectronic applications that use quantum dots.

Address correspondence to Shixuan Du, sxdu@iphy.ac.cn; Xinliang Feng, feng@mpip-mainz.mpg.de

1 Introduction

Graphene nanoribbons (GNRs) are considered the most promising building blocks for future graphene-based electronic devices [1–7] because of their tunable band gaps, which are thought to be determined by their widths, edge geometries, and dopants [8–16]. For example, a variety of armchair GNRs with different widths has recently been fabricated via a surface-assisted reaction [8, 11, 17]. However, controlling the band structures of GNRs using their widths remains a challenge because the availability of suitable laterally extended monomers is limited [18, 19].

Chevron-type pristine or nitrogen-doped GNRs (N-GNRs) have been successfully synthesized via surface-assisted polymerization of dibromosubstituted oligophenylene monomers with or without nitrogen atoms, followed by intramolecular cyclodehydrogenation [17, 20]. The arrangement of four N atoms in the oligophenylene monomer (Fig. 1(a)) is axisymmetric so that N is incorporated uniformly along the backbones of the resulting GNRs. However, such a configuration can only lead to shifting the band alignment without changing the band gap magnitude [17, 20].

In the present work, we report that sulfur-substituted monomers (6,11-dibromo-1,4-diphenyl-2,3-di-(thien-3-yl)-triphenylene, Fig. 1(b)), on a Au (111) substrate can evolve into sulfur-containing GNRs (S-GNRs) with tunable band gaps. In contrast to the N-substituted oligophenylene monomer, this sulfur-substituted monomer allows a family of distinct cyclodehydrogenated constitutional isomers to be derived via intramolecular cyclization at different sites [5]. Density functional theory (DFT) calculations show that these cyclodehydrogenated constitutional isomers can exhibit distinct highest occupied molecular orbital (HOMO)–lowest unoccupied molecular orbital (LUMO) gaps. Due to the versatility of the sulfur-substituted monomers, this feature offers a basis for construction of GNRs consisting of a sequence of quantum dots (Fig. 1(b)) [21]. Such unique GNRs have been confirmed via scanning tunneling microscopy (STM) and scanning tunneling spectroscopy (STS). Other isomeric oligophenylene monomers with S atoms at different sites can be designed and may result in S-GNRs with controllable band gaps. Thus, the present approach

offers a simple way to perform band gap engineering using a single type of oligophenylene monomer.

2 Results and discussion

When deposited on a Au (111) substrate, the sulfur-substituted monomer has three unequal configurations (isomers 1-a, 1-b, and 1-c in Fig. 1(b)) because substrate interactions restrict the rotation of the two thienyl rings. Isomers 1-a and 1-b are the most centrosymmetric of the three. In projection, both sulfur atoms point to the same side. In isomer 1-c, the sulfur atoms are oriented differently and no symmetry axis is present. After thermal activation, the carbon–bromine bonds break simultaneously (debromination) and some hydrogen atoms detach from the carbon atoms (dehydrogenation), facilitating formation of carbon–carbon bonds between two neighboring monomers (cyclization) [5, 15, 17]. Six possible cyclodehydrogenated constitutional isomers from 1-a' to 1-c'' can be derived, are shown in Fig. 1(b). The bonds formed by cyclization between thienyl rings and their neighbors are marked in red and blue respectively.

DFT calculations show that the six cyclodehydrogenated constitutional isomers presented in Fig. 1(b) have different HOMO–LUMO gaps, which range from 2.14 to 2.56 eV. The band gap of this new class of S-GNRs is determined primarily by its different cyclization sites, α -C (the nearest carbon to sulfur in the thienyl ring, with a bond marked with a red shadow) and β -C (the second-nearest carbon to sulfur in the thienyl ring, with a bond marked with a blue shadow). Both isomers 1-a' and 1-c' cyclize at α -C on the left thienyl ring but no cyclization occurs on the right one.

The HOMO–LUMO gaps of these two cyclodehydrogenated isomers are similar (2.41 eV and 2.46 eV, respectively). However, 1-b' has a larger HOMO–LUMO gap (2.56 eV), with cyclization at β -C on the left thienyl ring. These different HOMO–LUMO gaps caused by different cyclization sites lead us to infer that isomers with cyclization at α -C should have smaller HOMO–LUMO gaps than those with cyclization at β -C. Further cyclization of the right thienyl ring leads to the formation of three more constitutional isomers: 1-a'', 1-b'', and 1-c''. We expect that 1-a'' should

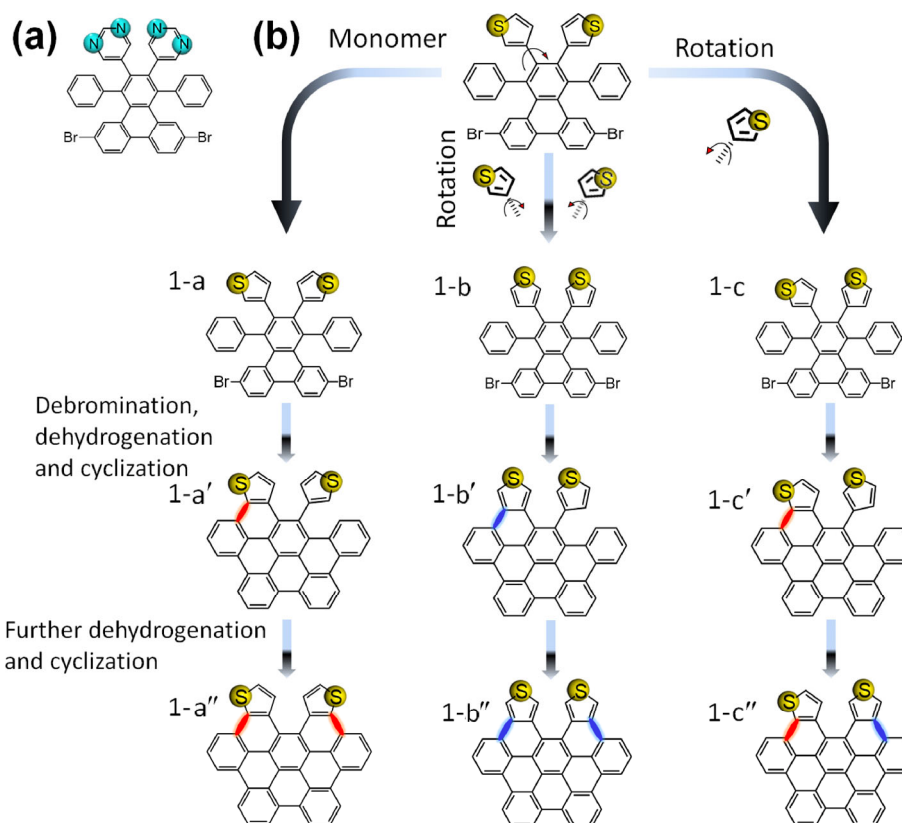


Figure 1 Monomer, isomer, and cyclodehydrogenated isomer structures. (a) Oligophenylene monomer with four nitrogen atoms. (b) Oligophenylene monomer with two thienyl rings. 1-a, 1-b, and 1-c are three distinct isomers of the monomer. The lower two lines show each of the three possible cyclodehydrogenated constitutional isomers after debromination, dehydrogenation, and cyclization of the monomer. The C–C bonds in red and blue are formed at α -C (ortho position to the S atom in a thienyl ring) or β -C (meta position to the S atom in a thienyl ring). Isomers 1-a', 1-b', and 1-c' only have one new bond for two thienyl rings, while 1-a'', 1-b'', and 1-c'' have two new bonds.

have the smallest HOMO–LUMO gap and 1-b'' the largest, with 1-c'' in the middle, organized by their cyclization sites (α -C or β -C). DFT calculations suggest the same sequence of HOMO–LUMO gaps: The HOMO–LUMO gaps for 1-a'' (cyclized at two α -C sites), 1-b'' (cyclized at two β -C sites), and 1-c'' (with one cyclized at an α -C site and the other at a β -C site) are 2.14, 2.38, and 2.25 eV, respectively. The distinct HOMO–LUMO gaps of these constitutional isomers enable opportunities to create new GNR heterojunctions simply by maneuvering constitutional isomers.

Figure 2 illustrates the process of fabricating S-GNRs by depositing sulfur-substituted monomers (synthetic details of the monomer are provided in methods) onto a Au (111) substrate (Fig. 2(a)). The thienyl rings in the monomers rotate during their deposition on the Au (111) surface, forming three different types of isomers due to the two-dimensional restriction of

the substrate. At first, the monomers aggregate into clusters on the Au (111) substrate (Fig. 2(b)). When the temperature increases, the isomers debrominate, polymerize, and cyclodehydrogenate into S-GNRs (Fig. 2(c)) [11, 15, 17].

Figure 3 displays STM images of monomers and the resulting chevron-type GNRs on a Au (111) substrate in an ultra-high vacuum (UHV) chamber. The monomers prefer to assemble together to form molecular clusters when deposited on substrates at room temperature (Fig. 3(a)). Higher-resolution imaging (Fig. 3(b)) confirms that these small clusters consist of isolated monomers. Figure 3(c) is a schematic that corresponds to the cluster marked by a green box in Fig. 3(b). After annealing at 450 °C, S-GNRs with lengths of tens of nanometers can form (Fig. 3(d)). All S-GNRs manifest similar topographies (the chevron structure) when compared to other all-carbon

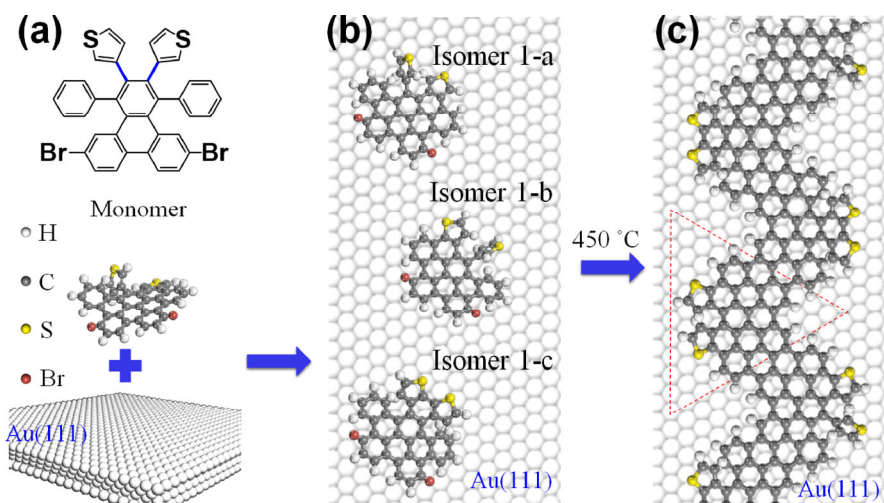


Figure 2 Bottom-up fabrication of S-GNRs. (a) Configuration of the monomer. (b) Monomers deposited onto an Au (111) substrate. Distinct isomers are present due to the rotation of the thiophene rings. (c) Schematic of S-GNRs on an Au (111) substrate.

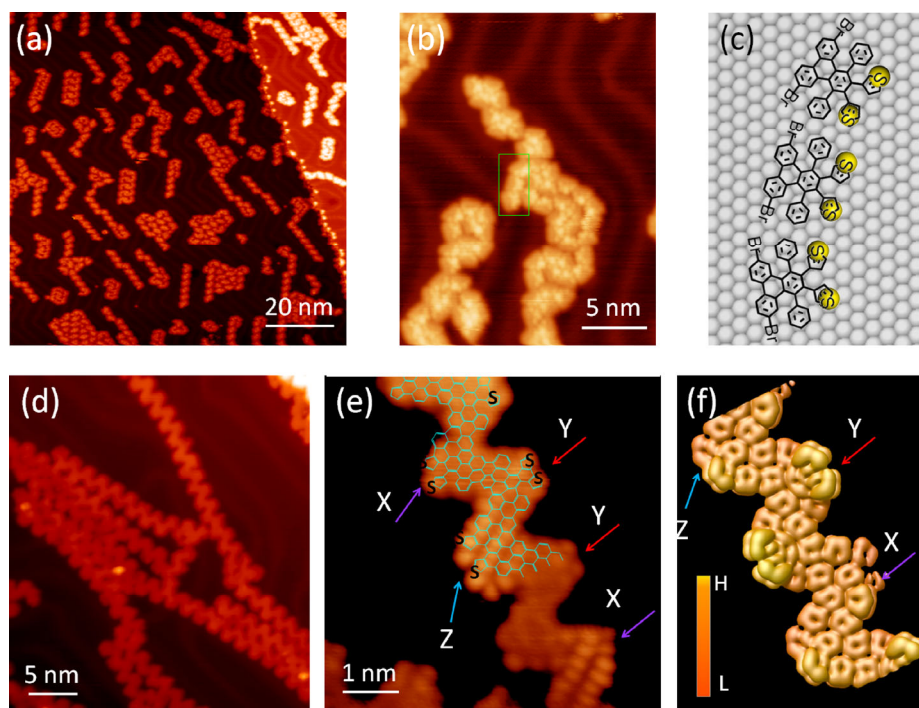


Figure 3 STM images of monomers on Au (111) before and after polymerization and cyclodehydrogenation. (a) STM image of monomers deposited separately on the Au (111) substrate ($U_{\text{bias}} = -3.0$ V, $I_t = 0.05$ nA). (b) Magnified image of (a). (c) Schematic of the structure in the green box in (b). (d) Large area STM image of the nanoribbons after annealing at 450 °C ($U_{\text{bias}} = -3.0$ V, $I_t = 0.05$ nA). (e) High-resolution STM image of S-GNRs with a partly overlaid structural model ($U_{\text{bias}} = -0.3$ V, $I_t = 1.00$ nA). (f) STM simulation image of the lower part of the S-GNRs in (e).

chevron-type GNRs [17]. However, the high-resolution STM image can reveal some fine structural details. Figure 3(e) shows one representative high-resolution STM image, overlaid with a structural model of the ribbons. One prominent feature can immediately be

identified: the GNRs exhibit different levels of image contrast, which suggests that the local density of states (LDOS) is not uniform.

Due to the different S positions and cyclization positions, there are 17 possible distinct S-doped

graphene nanoribbon segments. A high-resolution STM image (Fig. 3(e)) clearly shows three distinct segments with different structural characteristics: one protrusion, two identical protrusions, and a complex feature, labeled X, Y, and Z, respectively. By using just three types of segments, we constructed a possible S-GNR in Fig. 3(e). The resulting STM simulation (Fig. 3(f)) shows similar features with the experimental results.

Only one protrusion can be observed at the position with two thienyl groups in segment X of the S-GNRs. This is probably due to the non-coplanar nature of the two thienyl rings (caused by steric hindrance from the nearest H atoms). That is, one of the thienyl rings is far away from the Au (111) substrate, while the other is close. Hence, only the LDOS of the raised ring contributes to the protrusion shown in the STM images. The two thienyl rings in segment Y exhibit two protrusions with identical heights. This suggests that the two thienyl rings have the same geometric structure and LDOS. In the STM image, the features of segment Z are more asymmetric than those of

segment Y. Based on the above analysis, we propose an S-GNR structure that can explain the STM topography (Fig. 3(e)). The corresponding simulated STM image (Fig. 3(f)) agrees with the experimental observations (Fig. 3(e)).

We have also performed low-temperature STS measurements (4.2 K) to determine the different electronic structures of various segments in the GNRs (Fig. 4(a)). Figure 4(b) shows three selected dI/dV spectra marked in red, cyan, and magenta, acquired from sites 1, 4, and 5 in Fig. 4(a), respectively. A spectrum recorded on a bare Au (111) substrate (black curve) with the same tip is shown for comparison and used as the background. It exhibits the characteristic surface-state-induced Au (111) peak (indicated by the black arrow).

As expected, each GNR spectrum exhibits two peaks near the Fermi level. These peaks are marked with dashed lines. One is located below the Fermi energy (E_F) while the other is located above E_F . They can be interpreted as the valence and conduction band

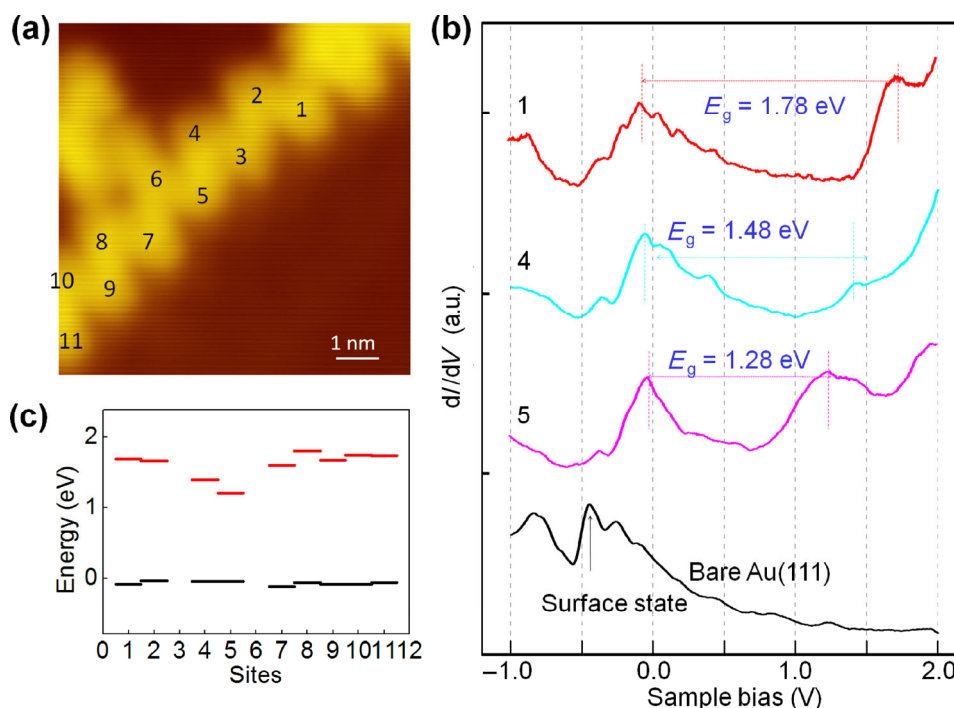


Figure 4 Electronic structures of the S-GNRs. (a) STM images of the S-GNRs. STS data were obtained from different sites (marked 1 through 11). (b) dI/dV spectra measured on bare Au (111) (black) and S-GNRs. Red, cyan, and magenta curves correspond to the spectra taken at sites 1, 4, and 5 marked in (a), respectively. The spectra are vertically offset for clarity. (c) Band edge distribution at different S-GNR sites in (a). VBE (short black lines) and CBE (short red lines) are the corresponding valence and conduction band edges. The band edges of sites other than 3 and 6 represent a statistical average calculated from twenty measurements. The tip exhibits abnormal behavior on sites 3 and 6. Thus, data on these two sites is missing.

edges (VBE & CBE), respectively. Thus, the energy difference between them is the band gap (E_g). It is clear from comparison of dI/dV spectra recorded at different sites that the CBEs and VBEs are variable. In spectrum 1 (red curve), the CBE and VBE are located at 1.69 and -0.09 V, respectively. Hence, the band gap is $E_g = 1.78$ eV. In spectra 4 and 5 (cyan and magenta curves), the CBEs and VBEs both shift close to E_F in sequence with their counterparts in spectrum 1. Their E_g values are 1.48 and 1.28 eV, respectively.

Figure 4(c) summarizes the band gap magnitudes measured along different sites in the ribbon. All of the STS data are calculated from the averages of 20 measurements at each site. The band gap varies from 1.28 to 1.87 eV. This band gap evolution confirms the presence of quantum dots.

Qualitatively, our DFT calculations for a single S-GNR (Fig. 5(a)) composed of various segments support the conclusions that we have made from our experimental data. As observed via STS measurements, the projected local densities of states (PDOS) of distinct segments are different (Fig. 5(b)). While the

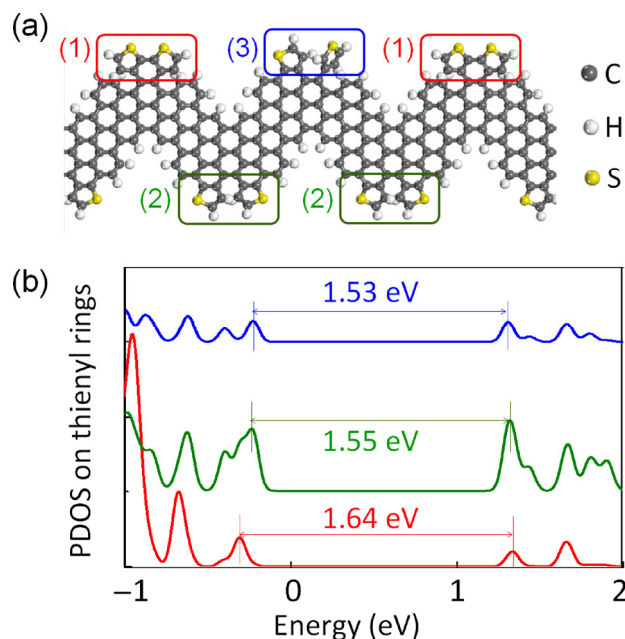


Figure 5 Schematic structures and the corresponding calculated PDOSs of S-GNRs composed of distinct segments. (a) S-GNR composed of three distinct segments, marked in red (1), green (2), and blue (3). (b) PDOSs of distinct segments in the S-GNR. The red, green, and blue lines correspond to the PDOSs of segments (1), (2), and (3), respectively, in (a). The green and blue curves are vertically offset for clarity.

experimental tendency towards band gap variation qualitatively aligns with the theoretical results, there is a discrepancy between the predicted and experimental band gap magnitudes. Such a discrepancy is likely because: (1) The theoretical calculations are based on calculations from free-standing GNRs, while the Au (111) substrate apparently influences the band gap values; and (2) the generalized-gradient approximation is used for calculations, which typically leads to underestimation of calculated band gaps.

3 Conclusions

In summary, S-substituted chevron-type GNRs composed of segments with various structures have been fabricated on a Au (111) substrate via a bottom-up synthetic approach. S-substituted oligophenylene monomers were used as the precursors. Unlike with the N-GNRs described in previous papers, a tunable S-GNR band gap can be produced due to the versatile monomer precursor configurations available during deposition and polymerization. This has been confirmed via both experimental STM/STS characterization and theoretical DFT calculations. Our development of S-GNRs with tunable band gaps determined via bond rotation of the monomer configuration can be generalized and extended to other systems. This may therefore offer novel bottom-up synthetic routes for band gap engineering of functional GNRs in the future.

4 Methods

4.1 Details of the theoretical calculations

Density functional theory calculations were performed using the Perdew–Burke–Ernzerhof (PBE) generalized gradient approximation [22]. The Vienna *ab initio* simulation package [23, 24] was used to perform the structural relaxations and band-structure calculations. The wave functions were expanded using a plane-wave basis set with an energy cutoff of 400 eV. The vacuum was set to 15 Å to avoid interactions between neighboring nanoribbons. The reciprocal space was sampled at the Γ point during optimization of each segment and the graphene nanoribbon. The band structure was calculated along high symmetry

directions in the Brillouin zone. The STM images were simulated using the Tersoff–Hamann approach [25].

4.2 Experimental details

The monomer was prepared via a modified Diels–Alder reaction procedure [26]: 5,10-Dibromo-1,3-diphenyl-2H-cyclopenta[1]phenanthren-2-one was reacted with 1,2-di(thien-3-yl)acetylene or 1,2-di(thien-2-yl)acetylene in diphenyl ether at 250 °C for 12 h. Purification via column chromatography (eluent: hexane-dichloromethane (DCM) mixtures) and recrystallization from DCM layered with ethanol generated the compounds as colorless solids. For the detailed synthetic protocol and analytical data, please see the Electronic Supplementary Material (ESM) (Table S1 and Fig. S2). The structures were unambiguously confirmed via single crystal X-ray analysis (Fig. S3 in the ESM).

All of the STM and STS experiments were performed under ultra-high vacuum with a base pressure of less than 1×10^{-10} mbar. The Au (111) surface was cleaned using cycles of argon-ion sputtering and annealing to 450 °C. The monomers were thermally evaporated onto the Au (111) substrate, which was kept at room temperature during evaporation. Topographic images of the GNRs were obtained in constant-current mode using a commercial Omicron low-temperature STM operating at 78 K. The STS curves were measured using a commercial Unisoku LT-STM at 4.2 K. A lock-in technique with sinusoidal modulation of 5 mV_{rms} at a frequency of 973 Hz was used during the spectroscopy measurements. The bias was applied to the sample. Electrochemically etched tungsten tips were used for all STM experiments.

Acknowledgements

Work at IOP and UCAS was supported by grants from the National Key Research and Development Program of China (No. 2016YFA0202300), the National Natural Science Foundation of China (Nos. 61390501, 61471337, 51210003, and 51325204), National Basic Research Program of China (No. 2013CBA01600), the CAS Pioneer Hundred Talents Program, the Trans-regional Collaborative Research Center TRR 61, and

the Chinese Academy of Sciences and the National Supercomputing Center in Tianjin. A portion of the research was performed in CAS Key Laboratory of Vacuum Physics. Work at the Max Planck Institute for Polymer Research were supported by the EC graphene flagship (No. CNECT-ICT-604391) and ERC NANOGRAPH. Work at Vanderbilt University was supported by Department of Energy grant DE-FG02-09ER46554 and by the McMinn Endowment.

Electronic Supplementary Material: Supplementary material (projected density of states of S-GNRs together with fabrication and the molecule information of sulfur-substituted monomer) is available in the online version of this article at <https://doi.org/10.1007/s12274-017-1550-2>.

References

- [1] Dutta, S.; Pati, S. K. Novel properties of graphene nanoribbons: A review. *J. Mater. Chem.* **2010**, *20*, 8207–8223.
- [2] Kim, W. Y.; Kim, K. S. Prediction of very large values of magnetoresistance in a graphene nanoribbon device. *Nat. Nanotechnol.* **2008**, *3*, 408–412.
- [3] Koch, M.; Ample, F.; Joachim, C.; Grill, L. Voltage-dependent conductance of a single graphene nanoribbon. *Nat. Nanotechnol.* **2012**, *7*, 713–717.
- [4] Li, X. L.; Wang, X. R.; Zhang, L.; Lee, S. W.; Dai, H. J. Chemically derived, ultrasmooth graphene nanoribbon semiconductors. *Science* **2008**, *319*, 1229–1232.
- [5] Shifrina, Z. B.; Averina, M. S.; Rusanov, A. L.; Wagner, M.; Müllen, K. Branched polyphenylenes by repetitive Diels–Alder cycloaddition. *Macromolecules* **2000**, *33*, 3525–3529.
- [6] Wu, X. J.; Zeng, X. C. Sawtooth-like graphene nanoribbon. *Nano Res.* **2008**, *1*, 40–45.
- [7] Bets, K. V.; Jakobson, B. I. Spontaneous twist and intrinsic instabilities of pristine graphene nanoribbons. *Nano Res.* **2009**, *2*, 161–166.
- [8] Huang, H.; Wei, D. C.; Sun, J. T.; Wong, S. L.; Feng, Y. P.; Castro Neto, A. H.; Wee, A. T. S. Spatially resolved electronic structures of atomically precise armchair graphene nanoribbons. *Sci. Rep.* **2012**, *2*, 983.
- [9] Son, Y. W.; Cohen, M. L.; Louie, S. G. Energy gaps in graphene nanoribbons. *Phys. Rev. Lett.* **2006**, *97*, 216803.
- [10] Yang, L.; Park, C. H.; Son, Y. W.; Cohen, M. L.; Louie, S. G. Quasiparticle energies and band gaps in graphene nanoribbons. *Phys. Rev. Lett.* **2007**, *99*, 186801.

- [11] Chen, Y. C.; de Oteyza, D. G.; Pedramrazi, Z.; Chen, C.; Fischer, F. R.; Crommie, M. F. Tuning the band gap of graphene nanoribbons synthesized from molecular precursors. *ACS Nano* **2013**, *7*, 6123–6128.
- [12] Ritter, K. A.; Lyding, J. W. The influence of edge structure on the electronic properties of graphene quantum dots and nanoribbons. *Nat. Mater.* **2009**, *8*, 235–242.
- [13] Bronner, C.; Strelau, S.; Gille, M.; Brauße, F.; Haase, A.; Hecht, S.; Tegeder, P. Aligning the band gap of graphene nanoribbons by monomer doping. *Angew. Chem., Int. Ed.* **2013**, *52*, 4422–4425.
- [14] Martins, T. B.; Miwa, R. H.; da Silva, A. J. R.; Fazzio, A. Electronic and transport properties of boron-doped graphene nanoribbons. *Phys. Rev. Lett.* **2007**, *98*, 196803.
- [15] Zhang, Y.; Zhang, Y. F.; Li, G.; Lu, J. C.; Lin, X.; Du, S. X.; Berger, R.; Feng, X. L.; Müllen, K.; Gao, H. J. Direct visualization of atomically precise nitrogen-doped graphene nanoribbons. *Appl. Phys. Lett.* **2014**, *105*, 023101.
- [16] Li, Y. F.; Zhou, Z.; Shen, P. W.; Chen, Z. F. Spin gapless semiconductor-metal-half-metal properties in nitrogen-doped zigzag graphene nanoribbons. *ACS Nano* **2009**, *3*, 1952–1958.
- [17] Cai, J. M.; Ruffieux, P.; Jaafar, R.; Bieri, M.; Braun, T.; Blankenburg, S.; Muoth, M.; Seitsonen, A. P.; Saleh, M.; Feng, X. L. et al. Atomically precise bottom-up fabrication of graphene nanoribbons. *Nature* **2010**, *466*, 470–473.
- [18] Narita, A.; Feng, X. L.; Müllen, K. Bottom-up synthesis of chemically precise graphene nanoribbons. *Chem. Rec.* **2015**, *15*, 295–309.
- [19] Narita, A.; Verzhbitskiy, I. A.; Frederickx, W.; Mali, K. S.; Jensen, S. A.; Hansen, M. R.; Bonn, M.; De Feyter, S.; Casiraghi, C.; Feng, X. L. et al. Bottom-up synthesis of liquid-phase-processable graphene nanoribbons with near-infrared absorption. *ACS Nano* **2014**, *8*, 11622–11630.
- [20] Liang, L. B.; Meunier, V. Atomically precise graphene nanoribbon heterojunctions for excitonic solar cells. *J. Phys. Chem. C* **2015**, *119*, 775–783.
- [21] Chen, Y. C.; Cao, T.; Chen, C.; Pedramrazi, Z.; Haberer, D.; de Oteyza, D. G.; Fischer, F. R.; Louie, S. G.; Crommie, M. F. Molecular bandgap engineering of bottom-up synthesized graphene nanoribbon heterojunctions. *Nat. Nanotechnol.* **2015**, *10*, 156–160.
- [22] Perdew, J. P.; Burke, K.; Ernzerhof, M. Generalized gradient approximation made simple. *Phys. Rev. Lett.* **1996**, *77*, 3865–3868.
- [23] Kresse, G.; Furthmüller, J. Efficiency of *ab-initio* total energy calculations for metals and semiconductors using a plane-wave basis set. *Comp. Mater. Sci.* **1996**, *6*, 15–50.
- [24] Kresse, G.; Hafner, J. *Ab initio* molecular dynamics for liquid metals. *Phys. Rev. B* **1993**, *47*, 558–561.
- [25] Tersoff, J.; Hamann, D. R. Theory of the scanning tunneling microscope. *Phys. Rev. B* **1985**, *31*, 805–813.
- [26] Saleh, M.; Baumgarten, M.; Mavrinskiy, A.; Schäfer, T.; Müllen, K. Triphenylene-based polymers for blue polymeric light emitting diodes. *Macromolecules* **2010**, *43*, 137–143.